Reaction Chemistry & Engineering

ROYAL SOCIETY OF CHEMISTRY

PAPER

View Article Online
View Journal | View Issue

Cite this: *React. Chem. Eng.*, 2025, **10**, 1244

Hydride-mediated chemoselective C–H bond formation during benzoic acid hydrodeoxygenation on anatase TiO_2†

Mikyung Hwang,‡ Jeremy Hu,‡ Michael J. Janik and Konstantinos Alexopoulos *

Received 18th November 2024,
Accepted 3rd March 2025

DOI: 10.1039/d4re00561a

rsc.li/reaction-engineering

The chemoselective hydrogenation of benzoic acid to aromatic products such as benzaldehyde, benzyl alcohol, toluene, and benzene is studied on anatase TiO_2 (001) using density functional theory (DFT) and microkinetic modeling (MKM). Oxygen vacancy (O_{vac}) sites are more active for benzoic acid hydrogenation than fully oxidized surface regions, with a nearly 2.5 eV lower energy for the first C–H bond formation reaction to occur near O_{vac}. This favorable C–H bond formation mechanism on anatase TiO_2 occurs between hydrides (H^-) and monoanionic intermediates coadsorbed in O_{vac}. A steady-state microkinetic model is constructed using computed reaction energies and activation barriers to determine rates of product formation at different reaction temperatures. Product selectivities differ in distinct temperature ranges, caused by competition among reaction and product desorption steps. Sensitivity analysis shows which elementary steps significantly affect the overall benzoic acid hydrogenation activity and selectivity.

1. Introduction

The production of aromatic products such as benzaldehyde, benzyl alcohol, toluene, and benzene[1–3] has been of interest due to their versatility as commodity chemicals and intermediates in chemical and pharmaceutical industries.[4] The chemoselective hydrogenation of benzoic acid has previously been identified as an attractive route for the formation of these aromatic products.[1,2,5,6] Benzoic acid is a relatively inexpensive feedstock that can be sourced from a variety of waste products. For example, polyethylene terephthalate (PET) plastic waste pyrolysis produced benzoic acid as the major product.[7,8] Thus, finding methods to catalytically upgrade benzoic acid to value-added products could make diverting PET plastic waste from landfills economically more feasible.

Selectivity is a challenging issue for aromatic carboxylic acid hydrogenation,[9] since hydrogenating the aromatic ring is typically easier than preserving its aromaticity and exclusively hydrogenating the carboxyl group.[1,6,10,11] Although some studies have demonstrated promising results in achieving aromatic product selectivity, there remains considerable variation in both the distribution of products obtained and the proposed reaction mechanisms.[2,5,12,13] In principle, benzoic acid hydrogenation can produce aromatic products such as benzaldehyde, benzyl alcohol, benzene, and toluene (Fig. 1).[1] Notably, the carbon of the carboxyl group undergoes several C–H bond formation steps upon the consecutive hydrogenation of benzoic acid towards toluene. Meanwhile, benzene can be produced through the decarboxylation of benzoic acid[12,14] or the decarbonylation of benzaldehyde.[15,16] Benzene production *via* the demethylation of toluene appears unlikely as only CO and CO_2 (*i.e.*, no CH_4) are detected under relevant conditions.[17,18] Among the possible aromatic products of benzoic acid, hydrogenated products such as toluene and benzyl alcohol are often preferred over benzaldehyde due to their value-added demand as solvents and ester precursors.[14,19–21]

The development of a superior catalyst for the selective hydrogenation of benzoic acid, capable of achieving high selectivity for specific aromatic products, remains an active area of research.[6,9] Numerous studies focused on ring hydrogenation for cyclohexanecarboxylic acid production.[22–26] While some studies have reported supported metals such as Au[1,16,27] and Pt[2] to be selective for aromatic products, the specific role of oxide catalysts or supports in benzoic acid hydrogenation remains unclear. Early studies have reported high yields and selectivity for benzaldehyde on ZrO_2 (ref. 5 and 6) and CeO_2,[28] albeit at higher temperatures than on extended metal clusters. For example, benzoic acid hydrogenation on Au/CeO_2 was reported to occur at 573 K,[1]

Department of Chemical Engineering, The Pennsylvania State University, University Park, Pennsylvania, 16801, USA. E-mail: kxa5325@psu.edu

† Electronic supplementary information (ESI) available: Computational methods and details, alternative mechanisms of product formation, additional geometric details and configurations of reaction intermediates, overall reaction energy diagram, kinetic model parameters and differential equations, surface coverages, and detailed rate analysis. See DOI: https://doi.org/10.1039/d4re00561a

‡ Denotes equal authorship.

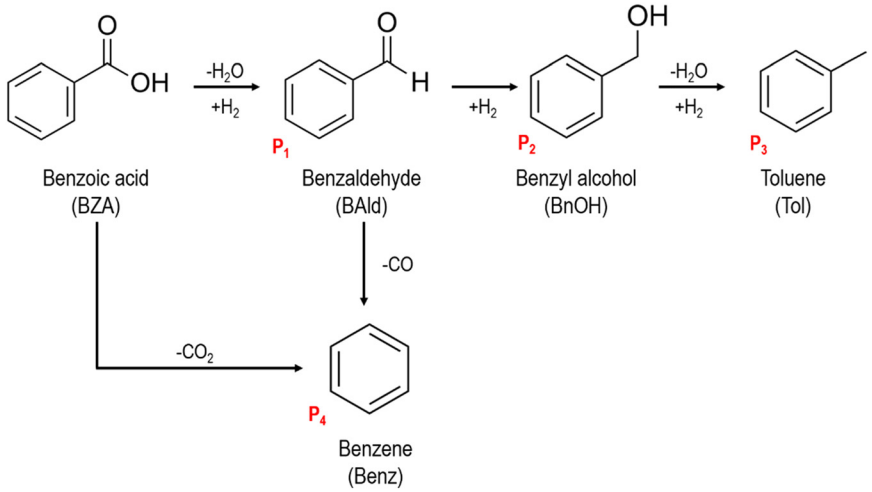

Fig. 1 Reaction scheme for the chemoselective hydrogenation of benzoic acid to aromatic products.

while activity on CeO_2 occurs between 523–723 K.[28] The only study of benzoic acid hydrogenation on TiO_2 reported lower selectivity for benzaldehyde and higher selectivity for toluene and benzene (*i.e.*, relative to HfO_2 and ZrO_2).[6] Ponec *et al.* hypothesized from their experiments on various metal oxides that the M–O bond strength and, by extension, the concentration of surface oxygen vacancy (O_{vac}) sites dictates the selectivity for benzaldehyde.[6,9,28] The same authors suggested mechanisms such as a reverse Mars and van Krevelen or radical-like benzoate decomposition as responsible for benzaldehyde formation.[9,28,29] To date, no *ab initio* studies have been published to provide atomistic confirmation of elementary reaction mechanisms or selectivity determining steps in benzoic acid hydrodeoxygenation (HDO) on metal oxides.

The search for highly selective catalysts for the chemoselective hydrogenation of complex aromatics is not exclusive to benzoic acid hydrogenation. Single-atom catalysts (SACs), with metals atomically dispersed on a support,[30,31] have emerged as remarkably selective catalysts for similar reactions. For example, Liu *et al.* reported highly active and selective Ag SACs on anatase TiO_2 for phenolic products from guaiacol, a biomass-derived aromatic (*i.e.*, aromatic products preferred over ring hydrogenation).[32] Both experimental and DFT studies confirm that the Ag single atoms serve as sites for H_2 activation and a source of continuous hydrogen spillover to the TiO_2 support.[32–34] Since single atom catalysts have the metal atomically dispersed on the surface at extremely low coverages[35,36] and because Ag is typically not active for hydrogenation,[32] the vast majority of hydrogenation reactions, such as C–H bond formation, is expected to occur on the TiO_2 surface (*i.e.*, whereas the metal mainly acts as a source of spillover H atoms).

Since hydrogenation conditions over metal oxides require temperatures above 523 K,[28] the presence of O_{vac} is expected on the oxide surface.[37,38] Nuclear magnetic resonance (NMR) results[39] as well as our previous work[33] on anatase TiO_2 have identified hydrides in O_{vac} as stable species of spillover H atoms when the surface is exposed to high temperature reducing conditions. Thus, in this paper, we use DFT and MKM to achieve two goals: 1) determine the mechanisms and selectivity of benzoic acid hydrodeoxygenation on anatase TiO_2, and 2) examine the roles and effects that O_{vac}-adsorbed hydrides have in the hydrodeoxygenation reaction in general and the C–H bond formation steps in particular.

2. Methods

2.1. Development of surface models

The (001) facet of anatase TiO_2, a low index facet of anatase considered to be the most active for catalytic reactions,[40–42] was used for this study. Periodic 2 × 2 supercells of (001) anatase were constructed with a vacuum region of 15 Å above the slab to minimize periodic dipole interactions normal to the surface. The slab is two layers thick, with each layer defined as the minimum depth of atoms to achieve Ti_nO_{2n} stoichiometry in the 2 × 2 supercell; each layer is comprised of three atomic sublayers (*i.e.*, six atomic layers in total to form a $Ti_{24}O_{48}$ unit cell). The three uppermost atomic layers are allowed to freely relax during geometric optimizations, while the bottom three layers are fixed in position to model the bulk anatase support (Fig. S1†). Atomic figures shown in this publication were constructed using the Amsterdam modeling suite (AMS).[43]

Surface oxygen atoms are characterized based on their local coordination, with oxygens coordinated to two and three Ti atoms referred to as O_{2C} and O_{3C}, respectively (Fig. 2a). O_{vac} readily form on the surface as a result of TiO_2 reduction (*i.e.*, two spillover H atoms combine with a surface O to desorb as H_2O and leave an O_{vac}).[44,45] Previous studies have established that bridging O_{2C} atoms require the least amount of energy to form a vacancy,[33,46] so models of the reduced TiO_2 (001) surface have an O_{2C} vacant (Fig. 2b).

2.2. Electronic structure methods

DFT was implemented through the Vienna *ab initio* simulation package (VASP)[47] using the Perdew–Burke–

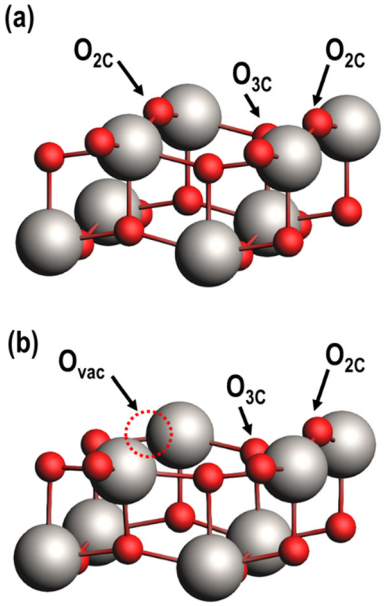

Fig. 2 The anatase TiO_2 (001) surface with (a) the fully oxidized surface having one pair each of O_{2C} and O_{3C}, and (b) a reduced surface with an O_{2C} substituted with an O_{vac}. Only the two uppermost atomic layers are shown for clarity. Ti (gray), O (red), and an O_{vac} (dashed circle) are depicted.

Ernzerhof (PBE) exchange correlation functional.[48] The projector augmented-wave (PAW) method was used to take into account core–valence interactions[49] and PBE + D3 was used to correct for dispersion interactions.[50,51] The self-interaction error from strongly correlated d-orbital electrons on Ti requires the use of DFT+U corrections on Ti.[52] The Hubbard's U parameter was set to 3 eV, as it was confirmed to give reasonable results for the energy of reduction of TiO_2 to Ti_2O_3 and was proposed for computing redox cycles on TiO_2 by Hu and Metiu.[53] During geometric optimizations, iterative calculations were considered converged when the forces on atoms reached less than 0.05 eV $Å^{-1}$. The self-consistent field tolerance was set to 10^{-5} eV. All calculations were spin-polarized. The Monkhorst–Pack k-point mesh of 3 × 3 × 1 and a plane-wave basis set cutoff energy of 450 eV were used.[54,55] Valence electrons considered for each atom type were Ti ($3s^2\ 3p^6\ 4s^1\ 3d^3$), O ($2s^2\ 2p^4$), C ($2s^2\ 2p^2$), and H ($1s^1$). Transition state searches were performed using the climbing image nudged elastic band method (CI-NEB), with the search considered converged when the transition state has a tangent force less than 0.05 eV $Å^{-1}$ and one imaginary vibrational frequency.

Adsorption energy of an absorbate to the TiO_2 surface (ΔE_{ads}) was calculated as:

$$\Delta E_{ads} = E_{adsorbate\_on\_surface} - E_{adsorbate} - E_{bare\_surface} \quad (1)$$

Here, $E_{adsorbate}$ is the gas phase adsorbate energy. Desorption energies are calculated from the adsorption energies as $\Delta E_{des} = -\Delta E_{ads}$. O_{vac} formation energies (ΔE_{vac}) were calculated with respect to gas phase H_2 and H_2O (eqn (2)).

$$H_2 + Ti_nO_{2n} \xrightarrow{\Delta E_{vac}} Ti_nO_{2n-1} + H_2O \quad (2)$$

Co-adsorption effects of two adsorbates, A and B, were quantified using a co-adsorption energy (ΔE_{CoAds}) respective to A and B co-adsorbed on the same O_{vac} site and the two adsorbates bound separately to O_{vac} site on individual reduced TiO_2 unit cells (Ti_nO_{2n-1}) (eqn (3)):

$$A\text{-}Ti_nO_{2n-1} + B\text{-}Ti_nO_{2n-1} \xrightarrow{\Delta E_{CoAds}} A,B\text{-}Ti_nO_{2n-1} + Ti_nO_{2n-1} \quad (3)$$

Zero-point vibrational energies (ZPVE) for all gas phase molecules and adsorbates were included to correct for the energy contribution of harmonic vibrational frequencies at 0 K.

2.3. Kinetic model development

A dual site microkinetic model (MKM) was constructed to predict the hydrogenation performance of anatase TiO_2 (001) at reaction conditions. Reduced TiO_2 sites were used to facilitate the C–H bond formation reactions occurring at O_{vac} (*), while spillover H atoms are sourced from fully oxidized regions away from the C–H bond formation sites (**). When H atoms are needed for each C–H bond formation step, the spillover H atoms are assumed to be continuously sourced from (**). The coordinates of all surface intermediates and transition states included in our MKM are provided in the Appendix within the ESI.†

A gas-phase reference adjustment is made for DFT adsorption and desorption energies in the MKM to match the overall thermodynamics to the NIST gas-phase thermodynamic values (see eqn (S1), Table S1†).[56,57] Entropy changes corresponding to adsorption or desorption of gas phase species were calculated using correlations available in the literature for standard gas phase absolute entropies as a function of temperature[58,59] and approximations of their entropies as adsorbed species developed by Campbell *et al.* (eqn (4)).[60] More specifically,

$$S^0_{ads}(T) = 0.70S^0_{gas}(T) - 3.3R \quad (4)$$

where $S^0_{ads}(T)$ is entropy of the adsorbed species at temperature T, and $S^0_{ads}(T)$ is gas-phase entropy at temperature T obtained from the NIST database. A comparison of adsorbed species entropies using different approaches (immobile, mobile and quasi-harmonic approximations)[61] for the main products including benzaldehyde, toluene and benzene is included in Fig. S2.† Additionally, the entropy of the desorption transition state at temperature T ($S^0_{TS,des}(T)$) was calculated as:

$$S^0_{TS,des}(T) = S^0_{ads}(T)/0.68 \quad (5)$$

Adsorption and desorption entropies are then defined as $\Delta S^0_{ads} = S^0_{ads} - S^0_{gas}$ and $\Delta S^0_{des} = S^0_{TS,des} - S^0_{ads}$, respectively. Using eqn (4)

may slightly overestimate the entropy loss of adsorbates that can dissociate such as H_2. Instead, ΔS^0_{ads} of H_2 dissociative adsorption is approximated as −47.7 J mol^{-1} K^{-1}, as reported by Vannice *et al.*[62] Entropy changes for reactions between surface intermediates are assumed to be negligible.

Equilibrium constants were calculated for each elementary step i using standard free energy changes (ΔG^0) that combine the re-referenced DFT energetics with the aforementioned approximations for the entropy changes (ΔS^0):[63,64]

$$K_{eq,i} = \exp\left(\frac{-\Delta G_i^0}{RT}\right) = \frac{k_i}{k_{-i}} \quad (6)$$

where T is the temperature, and R is the ideal gas constant. Reaction rate constants (k_i and k_{-i}) were calculated using the Eyring equation with the attempt frequency from transition state theory as the pre-exponential factor:[65,66]

$$k_i = \frac{k_B T}{h} \exp\left(\frac{-\Delta G_i^{0,\ddagger}}{RT}\right) \quad (7)$$

where k_B is the Boltzmann constant, h is the Planck constant, and $\Delta G^{0,\ddagger}$ is the standard free energy of activation as calculated from the re-referenced DFT energetics and the aforementioned approximations for the entropy changes (ΔS^0). For adsorption/desorption steps including the dissociative/associative adsorption/desorption of H_2, the rate constant was defined for the desorption direction using eqn 7, while the adsorption rate constant was calculated from the desorption rate constant and the equilibrium constant (eqn (6)). For the elementary steps involving only surface intermediates, transition states were only found for those deemed kinetically relevant, such as those involving C–H bond formation during HDO,[67,68] hydrogen shifts and C–C bond breaking during decarboxylation or decarbonylation.[69] For the rest of those steps, eqn (7) was used to define the rate constant in the endothermic direction by replacing the free energy of activation with the reaction energy in that direction, with the rate constant in the exothermic direction ending up as k_BT/h.

To determine surface coverages and reaction rates, a set of ordinary differential equations is setup (see eqn (S3) in ESI†) and integrated with time until steady state is reached, namely:

$$\frac{d\theta_j}{dt} = \sum_i \nu_{ij} r_i = 0 \quad (8)$$

where ν_{ij} is the stoichiometric coefficient of surface species j in reaction i and r_i is the net rate of reaction i. The relative selectivity of product p is referenced to the rates of production for all four products of interest (*i.e.*, benzaldehyde, benzyl alcohol, toluene, and benzene) (eqn (9)).[63]

$$Sel_p = \frac{r_p}{\sum_p r_p} \quad (9)$$

Sensitivity analysis of the product formation rates was performed with respect to individual kinetic rate constants using the degree of rate control (eqn (10)),[63,70,71] with each reaction rate constant perturbed by 2% and the rate of reactant consumption (*i.e.*, benzoic acid) taken to be the rate of interest.

$$X_{RC,i} = \left(\frac{\partial \ln r_{BZA}}{\partial \ln k_i}\right)_{k_{j\neq i}, K_i} \quad (10)$$

The partial equilibrium index (PEI) was calculated for each elementary reaction to gauge which steps are near equilibrium, thus not likely to be the rate determining step (eqn (11)).[72,73] A reaction step with a PEI between 0.45 and 0.55 is generally considered partially equilibrated.

$$PEI_i = \frac{r_{\vec{i}}}{r_{\vec{i}} + r_{\overleftarrow{i}}} \quad (11)$$

3. Results and discussion

3.1. Adsorption of benzoic acid on fully oxidized and reduced TiO_2

Both fully oxidized and reduced sites on anatase (001) will be present at high temperature hydrogenation conditions. This is evidenced by H_2O desorption and, by extension, O_{vac} formation during temperature programmed reduction (TPR)[6,32] and the presence of reduced Ti states using resonant photoemission spectroscopy.[74] DFT results quantified an O_{vac} formation energy of ΔE_{vac} = 1.57 eV on this (001) surface, while this energy decreases as low as ΔE_{vac} = 1.03 eV near Ag single atoms.[33] Thus, stable adsorption structures were determined for benzoic acid on both the fully oxidized and reduced (*i.e.*, with an O_{vac}) surfaces of anatase (001) (Fig. 3).

Benzoic acid molecular adsorption is thermodynamically favorable on both the fully oxidized (Fig. 3a) and reduced (Fig. 3d) surfaces, with ΔE_{ads} around −2 eV for both. On the O_{vac} surface, benzoic acid adsorbs into the vacancy with Ti–O bond formation between the O atoms of benzoic acid and each of the Ti atoms near the O_{vac}. This favorable adsorption state is 0.6 eV more stable than with a single O atom from benzoic acid bound in approximately the O_{vac} position (not shown). Dissociation of the hydroxyl group from benzoic acid is marginally more favorable on the fully oxidized (Fig. 3b) and reduced surfaces (Fig. 3e). However, dissociative adsorption of benzoic acid *via* deprotonation into an O_{vac}-bound benzoate anion and a proton on an O_{2C} was thermodynamically more favorable by 0.4 eV on the fully oxidized surface (Fig. 3c) and more than 1.5 eV on the reduced surface (Fig. 3f). These results agree well with studies which used infrared reflection-adsorption spectroscopy (IRRAS),[75] as well as scanning tunneling microscopy (STM) and low energy electron diffraction (LEED)[76] to confirm the spontaneous dissociative adsorption of benzoic acid to benzoate and hydroxyl groups on TiO_2. The deprotonated adsorption structure is consistent with previous DFT studies of benzoic acid adsorption.[77–79] Furthermore, carboxylic acid

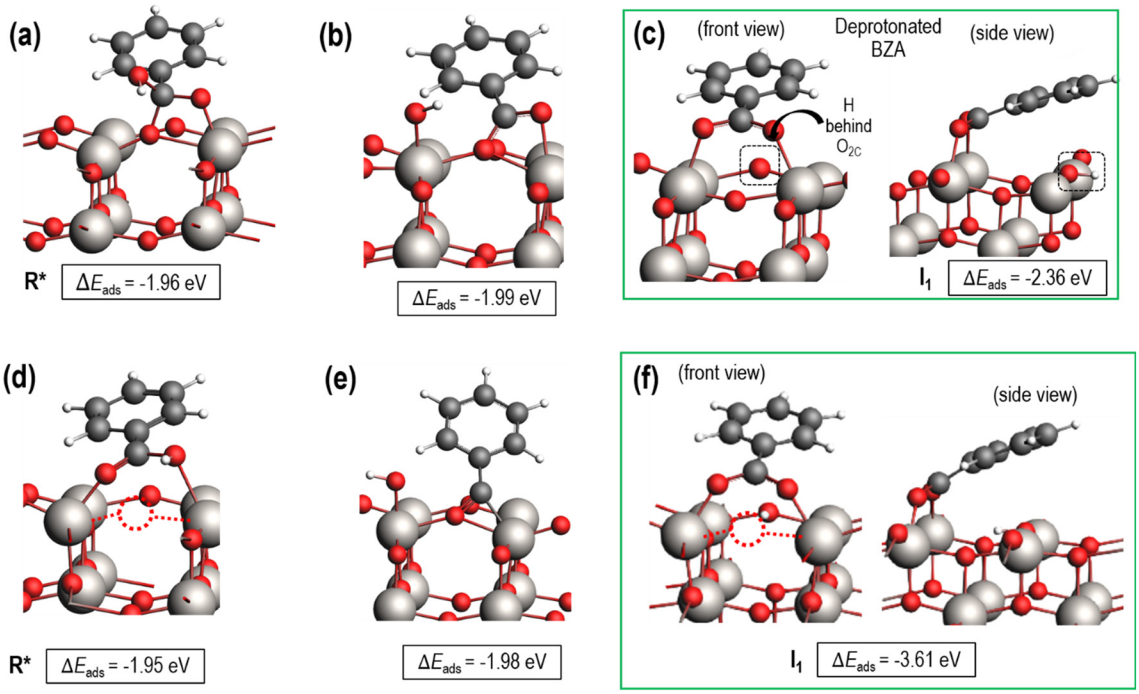

Fig. 3 Benzoic acid adsorption on fully oxidized and reduced anatase TiO_2 (001). Top row (a–c): Benzoic acid adsorbs on the fully oxidized surface either (a) molecularly, (b) dissociatively with the –OH group on a Ti atom, and (c) dissociatively by deprotonation. Bottom row (d–f): Benzoic acid adsorption on the reduced anatase TiO_2 (001) surface with an O_{vac} of an O_{2C} site. Stable structures included benzoic acid (d) molecular adsorption, (e) dissociative adsorption with –OH on a Ti atom, and (f) dissociative adsorption by deprotonation. R* and I_1 labels in a), c), d), and f) are referenced in Fig. 4. Ti (gray), O (red), C (black), H (white), and an O_{vac} (dashed circle) are depicted.

deprotonation on anatase TiO_2 is not only thermodynamically favorable but also essentially barrierless, with an experimental study reporting a barrier of around 0.05 eV for formic acid deprotonation on anatase (101) at 300 K.[80] Thus, further steps of hydrodeoxygenation are assumed to proceed from deprotonated, adsorbed benzoic acid on both the fully oxidized and reduced TiO_2 surfaces.

3.2. Benzoic acid hydrogenation to benzaldehyde on fully oxidized TiO_2 (001)

Stable structures were compiled along a plausible path of the first C–H bond formation of benzoic acid to benzaldehyde on the fully oxidized TiO_2 (001) surface. These structures and their relative energies were used to build a reaction energy diagram (Fig. 4). Starting with gas phase benzoic acid and the bare TiO_2 (001) surface, benzoic acid dissociatively adsorbs on the surface in its deprotonated form, as a benzoate anion and a H^+ (I_1, Fig. 3c). The H atom then migrates to the support O_{2C} near to the benzoate anion (I_2); I_2 is the most stable state compared to other structures of H adsorbed on atoms near the benzoate species. The first C–H bond formed (I_3) by H migration from O_{2C} to the carboxyl C proceeds uphill in energy by 3.98 eV. To close the catalytic cycle, a series of elementary steps follows, where O_{vac} is formed on O_{2C} next to the deprotonated phenylmethanediol (I_3), whose O atom refills the vacancy as a final step, producing benzaldehyde as a result of that step; the stepwise addition of 2 H atoms and desorption of O as H_2O (*i.e.*, $I_3 + 1/2H_2 \rightarrow I_4$ and subsequently $I_4 + 1/2H_2 \rightarrow P_1^* + H_2O$) occur favorably. The final adsorbed state is essentially an oxidized precursor of benzaldehyde (P_1^*). The desorption of benzaldehyde into the gas phase (P_1) reforms the fully oxidized TiO_2 surface and requires a reaction energy of 2.76 eV. Based on the reaction energy diagram of Fig. 4, *at least* 3.98 eV energy is required to form benzaldehyde from benzoic acid on the fully oxidized surface even without any kinetic barriers, indicating that this mechanism is too unfavorable to occur at relevant reaction temperatures.

3.3. Benzoic acid hydrogenation to benzaldehyde and decarboxylation to benzene on reduced TiO_2 (001)

The reaction energy profile of benzoic acid hydrogenation to benzaldehyde and decarboxylation to benzene on the reduced TiO_2 (001) surface with an O_{vac} was determined (Fig. 5). The relative energies are referenced to gas phase benzoic acid and the reduced TiO_2 (001) surface with an O_{vac}. Dissociative adsorption of benzoic acid into the benzoate anion (on the O_{vac}) and H^+ (on the O_{2C} opposite of the O_{vac}, I_1, Fig. 3f) is enthalpically favorable by 3.6 eV. The proton adsorbed on O_{2C} then migrates into the O_{vac}, forming a hydride species (I_2).[33,39] In effect, this state has two (−1) anions co-adsorbed in an O_{vac}, benzoate and H^-. The migration of H into O_{vac} to form two anionic species ($I_1 \rightarrow I_2$) proceeds uphill by 0.79 eV. The benzoate and hydride

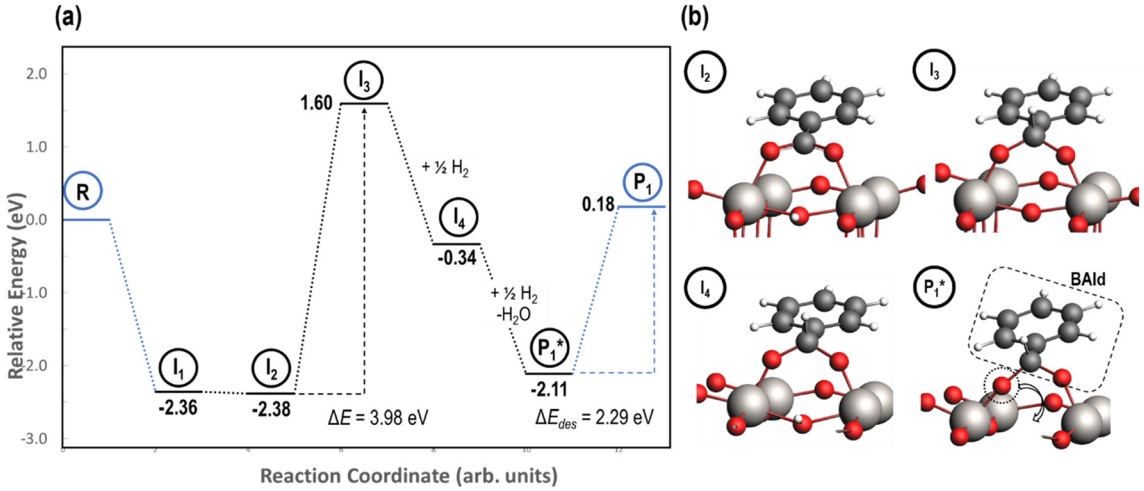

Fig. 4 Reaction energy diagram (a) with optimized intermediate structures (b) of benzoic acid hydrogenation to benzaldehyde on fully oxidized anatase TiO_2 (001). Stable intermediate I_1 corresponds to Fig. 3c. The energies of stable intermediates are referenced to gas phase benzoic acid and the fully oxidized TiO_2 (001) surface. Structures with gas phase molecules are circled in blue and adsorbed species in black. Only the uppermost atomic layer is shown for the sake of clarity. Ti (gray), O (red), C (black), and H (white) are depicted.

co-adsorption energy using eqn (3) is 0.58 eV, showing there is a repulsive interaction to placing two anionic ligands on the same O_{vac} site. From intermediate I_2, either C–H bond formation leading to benzaldehyde or decarboxylation leading to benzene can occur.

We first examine how intermediate I_2 may proceed to form benzaldehyde. The reaction between the hydride and benzoate in the vacancy results in a C–H bond formation ($I_2 \rightarrow I_3$), which proceeds downhill in reaction energy by 0.89 eV with a barrier of 0.64 eV. An alternate mechanism to form this first C–H bond was considered where H directly migrates from the O on benzoic acid to the C atom (R*, depicted in Fig. 3a, to I_3), forgoing both benzoic acid deprotonation and C–H bond formation *via* the anion-hydride mechanism (Fig. S3†). The activation barrier for this alternate mechanism is greater than 1 eV, suggesting that the hydride-mediated mechanism between the hydride and benzoate anion will be kinetically more favorable for C–H bond formation. Comparing relative rate constants for this competing path at a reaction temperature of 575 K (ref. 6) results in benzoic acid undergoing deprotonation nine orders of magnitude faster than C–H bond formation from the non-hydride route (eqn (S2)†). We also considered routes to C–H bond formation from which the H is passed to C from a surface O atom (not shown); however, these all proceed through either the hydride intermediate or by first placing the H onto the O atom of benzoate (*i.e.*, going back to molecularly adsorbed benzoic acid).

Once the C–H bond is formed through the hydride-mediated mechanism, structure I_3 can be considered as deprotonated phenylmethanediol. I_3 can further undergo hydrogenation to form benzaldehyde or decarboxylation to form benzene. In the case of hydrogenation, two H atoms are successively added on one of the O atoms of the deprotonated diol to form H_2O that desorbs. This leads to benzaldehyde adsorbed on O_{vac} ($I_3 + H_2 \rightarrow P_1^* + H_2O$), which proceeds thermodynamically uphill in energy by 0.99 eV. Finally, desorption of benzaldehyde from the O_{vac} surface requires more than 2.8 eV. Alternatively, benzaldehyde can first desorb from I_3 (oxidized precursor of benzaldehyde) by leaving one O in O_{vac} (refilling O_{vac}) followed by the reformation of O_{vac} (not shown).

Notably for the first C–H bond formation in benzoic acid, the required energy is at least 2.5 eV lower on the reduced surface than the fully oxidized surface (*i.e.*, compare 1.43 to 3.98 eV in Fig. 5 and 4, respectively). We conclude that carboxylic acid reduction on the TiO_2 surface will occur preferentially at O_{vac} sites. Therefore, further mechanistic steps (*i.e.*, hydrogenation of benzaldehyde, *etc.*) were considered on the TiO_2 surface with O_{vac}. The involvement of vacancy sites in the hydrodeoxygenation mechanism is supported by earlier experimental hypotheses that benzoic acid hydrogenation activity on reducible metal oxides increases with decreasing M-O bond strength (*i.e.*, higher O_{vac} concentrations).[6,28]

Instead of hydrogenation to benzaldehyde, decarboxylation to benzene can occur from benzoate intermediates.[81–83] Decarboxylation reactions have been well-documented on metal oxides and confirmed experimentally using IR spectroscopy and CO_2 desorption.[17] Starting with I_2, CO_2 can be eliminated from the adsorbed benzoate, resulting in a phenyl group co-adsorbed with a hydride in the O_{vac} ($I_2 \rightarrow I_{10} + CO_2$). Following the release of CO_2, a 0.46 eV activation barrier is required to form the C–H bond and produce benzene adsorbed on the O_{vac} (I_{10} to P_4^*). This C–H bond formation step to form benzene is thermodynamically favorable by 0.51 eV, with the desorption energy of benzene being 1.21 eV. Nonetheless, the energy barrier required to decarboxylate benzoate (at least 2.22 eV for I_2 to I_{10}) is higher than that required to hydrogenate benzoate (1.43 eV for I_2 to

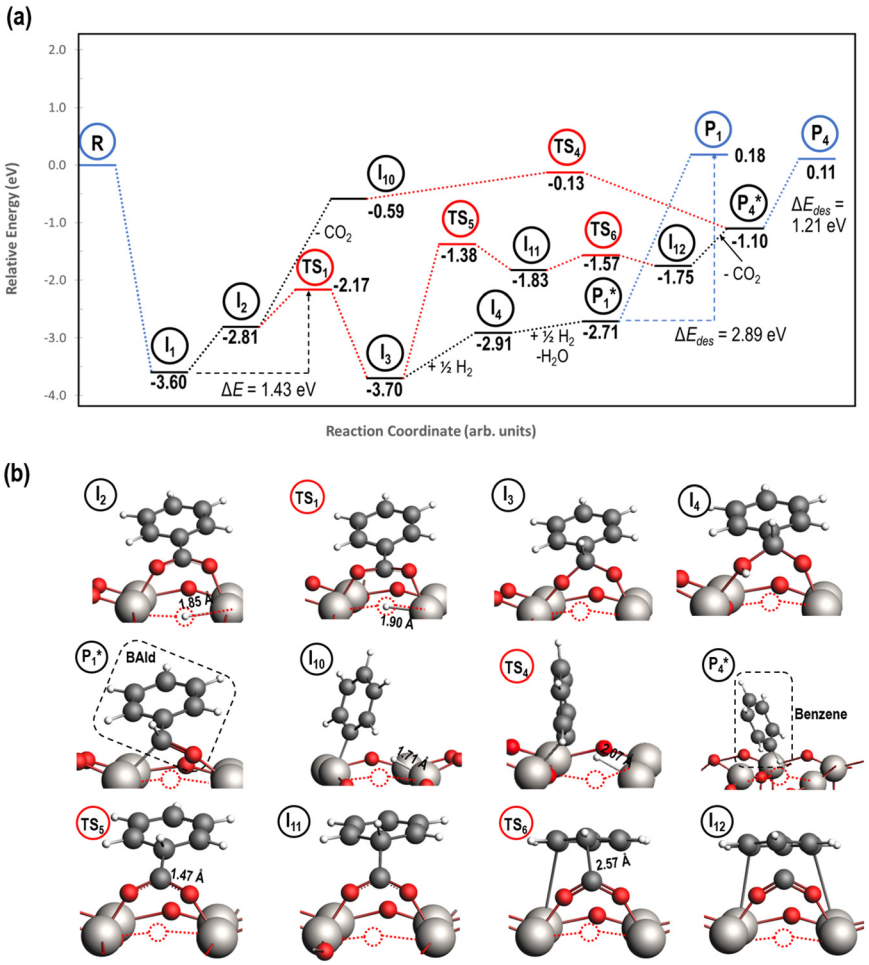

Fig. 5 Reaction energy diagram (a) with optimized intermediate structures (b) of benzoic acid hydrogenation to benzaldehyde and decarboxylation to benzene on reduced anatase TiO_2 (001) with an O_{vac}. Stable intermediate I_1 corresponds to Fig. 3f. All energies are referenced to gas phase benzoic acid and the reduced TiO_2 (001) surface. Structures with gas phase molecules are circled in blue, adsorbed species in black, and transition states in red. Only the uppermost atomic layer is shown for the sake of clarity. Ti (gray), O (red), C (black), H (white), and O_{vac} (dashed circle) are depicted.

I_3) on the reduced anatase TiO_2 (001) surface. Hence, we also considered a decarboxylation pathway from I_3.

This intermediate may undergo decarboxylation by shifting the hydrogen bound to the carbon of the carboxyl group to the carbon in the aromatic ring ($I_3 \rightarrow I_{11}$).[69] This hydrogen shift is an endothermic reaction with a barrier of 2.32 eV. Subsequently, the C–C bond between the carbon of the carboxyl group and the carbon in the aromatic ring can be broken, forming CO_2 and benzene adsorbed on the surface ($I_{11} \rightarrow I_{12}$). The energy barrier for this C–C bond breaking is 0.26 eV. The desorption energies for CO_2 and benzene are 0.65 eV and 1.21 eV, respectively. Nonetheless, I_3 needs to surpass a much higher energy barrier (2.32 eV for I_3 to I_{11}) on its way to decarboxylation than what is required for its further hydrogenation (0.99 eV for I_3 to P_1^*). Overall, these results indicate that it is energetically more favorable to hydrogenate benzoic acid to benzaldehyde on the reduced anatase TiO_2 (001) surface.

3.4. Benzaldehyde hydrogenation to benzyl alcohol and decarbonylation to benzene on reduced TiO_2 (001)

Next, the reaction path of benzaldehyde reduction to benzyl alcohol or benzene on the surface with an O_{vac} was considered (Fig. 6). The decarbonylation of benzaldehyde to form benzene is examined through a mechanism similar to a 1,2-hydrogen shift,[69,84,85] where the H atom migrates to an adjacent C atom ($P_1^* \rightarrow I_{13}$). The migration of H in this step requires an energy barrier of 2.04 eV. Subsequent C–C bond breaking, resulting in adsorbed CO and benzene molecules ($I_{13} \rightarrow I_{14}$), has a 0.42 eV energy barrier. Desorption of CO requires 0.86 eV, leaving benzene adsorbed on the O_{vac} (P_4^*). As a final step, benzene desorbs from the reduced surface, as already described in the decarboxylation pathways of the previous section.

Alternatively, benzaldehyde hydrogenation to benzyl alcohol requires additional O–H formation and C–H bond

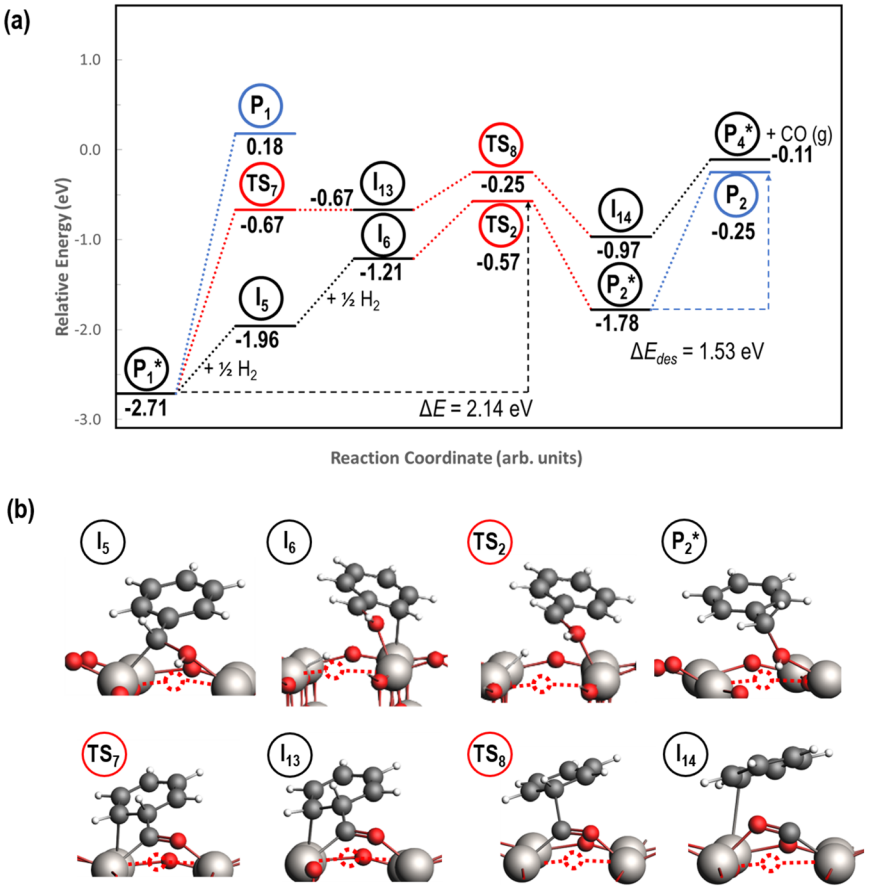

Fig. 6 Reaction energy diagram (a) with optimized intermediate structures (b) of benzaldehyde hydrogenation to benzyl alcohol on reduced anatase TiO_2 (001) with an O_{vac}. Structures with gas phase molecules are circled in blue, adsorbed species in black, and transition states in red. Only the uppermost atomic layer is shown for the sake of clarity. Ti (gray), O (red), C (black), H (white), and O_{vac} (dashed circle) are depicted.

formation. The addition of H to form the O–H bond proceeds uphill in reaction energy by 0.75 eV ($P_1^* \rightarrow I_5$), which ultimately forms a monoanionic ligand adsorbed on the O_{vac} (*i.e.*, benzyl alcohol missing a hydrogen on C). The subsequent co-adsorption of a hydride on the O_{vac} with the negatively charged ligand proceeds uphill by an additional 0.75 eV ($I_5 \rightarrow I_6$). However, the C–H bond formation from the co-adsorbed species, resulting in adsorbed benzyl alcohol ($I_6 \rightarrow P_2^*$), is exothermic and has the same barrier (*i.e.*, 0.64 eV) as the one reported in the previous section for the first C–H bond formation ($I_2 \rightarrow I_3$) *via* the hydride-mediated mechanism. Finally, benzyl alcohol has a desorption energy of 1.53 eV, which is 1.36 eV lower than the desorption energy of benzaldehyde. Nevertheless, an energy barrier of 2.14 eV (see Fig. 6) needs to be surpassed to hydrogenate adsorbed benzaldehyde (P_1^*) and form adsorbed benzyl alcohol (P_2^*), which is larger than the 1.43 eV hydrogenation energy barrier reported for benzaldehyde formation from benzoate (see Fig. 5). This is largely attributed to a higher co-adsorption energy of the monoanionic ligand (I_6) with the hydride in O_{vac} (ΔE_{CoAds} = 0.84 eV).

An alternate mechanism was explored for benzyl alcohol formation, reversing the order of H atom addition. The C–H bond is formed first, followed by the O–H bond to form benzyl alcohol (Fig. S4†). A hydride-mediated mechanism for C–H formation is no longer possible in this path, as the ligand co-adsorbed in the O_{vac} is neutral in charge (*i.e.*, benzaldehyde). Co-adsorption of a hydride with benzaldehyde in O_{vac} is significantly unfavorable (not shown), with a co-adsorption energy of more than 2.60 eV. Instead, the alternative mechanism forms the first C–H bond from a proton adsorbed on the O_{3C} of TiO_2 with a hydrogenation energy barrier (from S_1 to TS_{S1}) that is 0.21 eV lower than the one depicted in Fig. 6 (from P_1^* to TS_2). This result highlights that alternative mechanisms may be competitive with the hydride-mediated mechanism if anionic ligand repulsion leads to a high co-adsorption energy.

3.5. Benzyl alcohol hydrogenation to toluene on reduced TiO_2 (001)

A mechanism of benzyl alcohol hydrogenation to toluene is proposed in Fig. 7. The most energetically viable mechanism of toluene production (P_3^*) is directly from hydrogenating benzyl alcohol (P_2^*). The removal of the hydroxyl group from

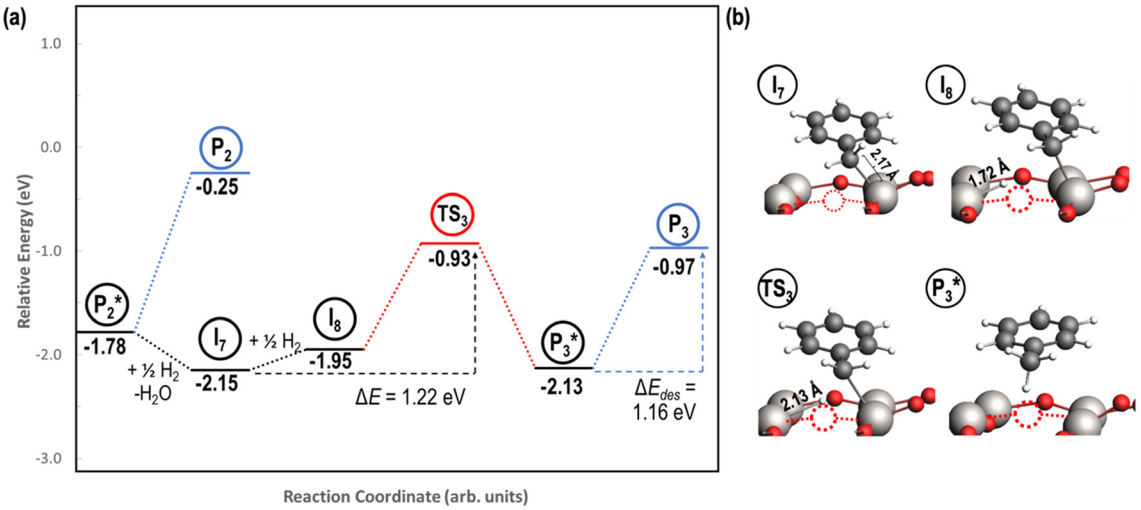

Fig. 7 Reaction energy diagram (a) with optimized intermediate structures (b) of benzyl alcohol hydrogenation to toluene (P_3^*) on reduced anatase TiO_2 (001) with an O_{vac}. Structures with gas phase molecules are circled in blue, adsorbed species in black, and transition states in red. Only the uppermost atomic layer is shown for the sake of clarity. Ti (gray), O (red), C (black), H (white), and O_{vac} (dashed circle) are depicted.

benzyl alcohol *via* the desorption of H_2O ($P_2^* \rightarrow I_7$) is thermodynamically favorable by 0.37 eV, leaving a benzyl ligand (I_7) adsorbed in the vacancy (*i.e.*, a monoanionic ligand). The addition of a hydride co-adsorbed into the vacancy ($I_7 \rightarrow I_8$) proceeds slightly uphill in reaction energy, attributed to a low co-adsorption energy of ΔE_{CoAds} = 0.28 eV between the two ligands (*i.e.*, only slightly net repulsive). Once again, the C–H bond formation to form toluene proceeds through a thermodynamically favorable reaction mechanism between a hydride and an electrophilic carbon center in a monoanionic ligand on an O_{vac}, with the reaction proceeding downhill by 0.18 eV ($I_8 \rightarrow P_3^*$). The energy barrier required to hydrogenate benzyl alcohol to toluene, 1.22 eV (Fig. 7), is the lowest compared to those of benzaldehyde and benzyl alcohol formation (Fig. 5 and 6, respectively). Finally, toluene has the lowest desorption energy compared to previous hydrogenation intermediates, suggesting that toluene may be a prominent gas phase product. Notably, the direct formation of toluene from benzaldehyde by bypassing the formation of benzyl alcohol is very unfavorable, since an energy barrier of 4.89 eV (see Fig. S5†) needs to be surpassed to hydrogenate adsorbed benzaldehyde (P_1^*) and form adsorbed benzyl (I_7).

Thus, C–H bonds consistently form through co-adsorbed hydrides and ligands that have −1 formal charges (*i.e.*, monoanionic ligands) bound in O_{vac}, with reasonably low kinetic barriers around or below 2 eV. The reaction energies of C–H bond formation between a hydride and the monoanionic species of interest (*e.g.*, benzoate, phenyl, benzyl) in an O_{vac} on TiO_2 are also consistently thermodynamically favorable. However, high reaction temperatures may still be necessary to form O_{vac} and to overcome barriers associated with the co-adsorption of two anionic species in O_{vac} (*i.e.*, ΔE_{CoAds}). Partial pressures of hydrogen and, by extension, surface H coverages under reduction conditions will also affect the rates of C–H bond formation.

3.6. Microkinetic model of benzoic acid hydrogenation in an O_{vac} site

A microkinetic model (MKM) that included reactions of H_2 dissociation, benzoic acid adsorption, sequential hydrogenation, decarboxylation or decarbonylation, and desorption of products, consisting of 24 elementary steps (Table 1), was constructed to predict the relative rates of product formation under reaction conditions using the DFT reaction energies and barriers (as summarized in Fig. S6a† and corrected by the values reported in Table S1†). The availability of H adsorbed on O sites (H**) is derived from H_2 heterolytic dissociative adsorption on the fully oxidized TiO_2 (001) surface (Fig. S7†), with a reaction energy of −0.33 eV and an energy barrier of 0.23 eV.

The detailed rate equations are described in eqn (S3).† The coupled system of 19 differential equations relating the rates of all intermediate surface species was solved simultaneously in the MKM. Gas phase concentrations were held constant, *i.e.*, $P_{H_2} = P_{BZA} = 1$ bar. Note that the presence of surface hydroxyls was not considered on the reduced surface with O_{vac} under the dry conditions in which we performed MKM, since the formation of these species is not favorable under these conditions according to the thermodynamic analysis shown in Fig. S8.† For reaction temperatures varying from 450 to 900 K, the formation rate of each product was calculated using the steady state concentrations of the surface intermediates (*i.e.*, Fig. S9b†). The steady state rates of benzaldehyde, benzyl alcohol, toluene, and benzene formation are shown as a function of reaction temperature in Fig. 8a. While the rates of product formation are negligible at low temperatures, an increase in T to 650 K brings the rates within an order of a magnitude difference from hydrogenation turnover frequencies on single atom catalysts.[86] For example, the experimental turnover frequency of guaiacol

Table 1 Elementary steps and reaction mechanism for hydrodeoxygenation, decarboxylation, and decarbonylation of benzoic acid on reduced anatase TiO_2 (001) surface. Equilibrated steps with partial equilibrium index between 0.45 and 0.55 at 540 K are indicated with circled arrow, and reaction steps with a degree of rate control higher than 0.1 at 540 K are indicated in bold

Product		Benz			BAld	BnOH	Tol
Path		D1	D2	D3	H1	H2	H3
0	$H_2\,(g) + 2^{**} \rightleftharpoons 2H^{**}$	0	0	1	1	1	1
1	$R(g) + * \rightleftharpoons I_1$	1	1	1	1	1	1
2	$I_1 \rightleftharpoons I_2$	1	1	1	1	1	1
3	$I_2 \rightleftharpoons I_3$	0	1	1	1	1	1
4	$I_3 + H^{**} \rightleftharpoons I_4 + {**}$	0	0	1	1	1	1
5	$I_4 + H^{**} \rightleftharpoons P_1^* + H_2O(g) + {**}$	0	0	1	1	1	1
6	$P_1^* \rightleftharpoons P_1(g) + *$	0	0	0	**1**	0	0
7	$P_1^* + H^{**} \rightleftharpoons I_5 + {**}$	0	0	0	0	1	1
8	$I_5 + H^{**} \rightleftharpoons I_6 + {**}$	0	0	0	0	1	1
9	$I_6 \rightleftharpoons P_2^*$	0	0	0	0	**1**	**1**
10	$P_2^* \rightleftharpoons P_2(g) + *$	0	0	0	0	1	0
11	$P_2^* + H^{**} \rightleftharpoons I_7 + H_2O(g) + {**}$	0	0	0	0	0	1
12	$I_7 + H^{**} \rightleftharpoons I_8 + {**}$	0	0	0	0	0	1
13	$I_8 \rightleftharpoons P_3^*$	0	0	0	0	0	1
14	$P_3^* \rightleftharpoons P_3(g) + *$	0	0	0	0	0	1
15	$I_2 \rightleftharpoons I_{10} + CO_2(g)$	1	0	0	0	0	0
16	$I_{10} \rightleftharpoons P_4^*$	1	0	0	0	0	0
17	$I_3 \rightleftharpoons I_{11}$	0	1	0	0	0	0
18	$I_{11} \rightleftharpoons I_{12}$	0	1	0	0	0	0
19	$I_{12} \rightleftharpoons P_4^* + CO_2(g)$	0	1	0	0	0	0
20	$P_1^* \rightleftharpoons I_{13}$	0	0	1	0	0	0
21	$I_{13} \rightleftharpoons I_{14}$	0	0	**1**	0	0	0
22	$I_{14} \rightleftharpoons P_4^* + CO(g)$	0	0	1	0	0	0
23	$P_4^* \rightleftharpoons P_4(g) + *$	1	1	1	0	0	0

Path D1/D2 (decarboxylation to Benz): R (g) ⇌ P_4 (g) + CO_2 (g)
Path D3 (decarbonylation to Benz): R (g) + H_2 (g) ⇌ P_4 (g) + H_2O (g) + CO (g)
Path H1 (hydrogenation to BAld): R (g) + H_2 (g) ⇌ P_1 (g) + H_2O (g)
Path H2 (hydrogenation to BnOH): R (g) + 2 H_2 (g) ⇌ P_2 (g) + H_2O (g)
Path H3 (hydrogenation to Tol): R (g) + 3 H_2 (g) ⇌ P_3 (g) + 2 H_2O (g)

hydrodeoxygenation on Ag_1/TiO_2 was determined to be near 10^{-3} s^{-1} at 573 K.[32]

Steady state rates of production were also used to calculate the relative selectivity of each product for the same temperature range (Fig. 8b). Two distinct temperature ranges are observed in the MKM, each of which has a specific product rate dominate. At low temperatures, the selectivity to toluene dominates over the selectivity to benzene and benzaldehyde. The small amount of benzene is formed through decarbonylation and not decarboxylation at these low T conditions as shown by a detailed rate analysis (Fig. S9a†). At higher temperatures, the selectivity to benzaldehyde consistently increases and is the highest amongst all products at temperatures of 540 K and above. Meanwhile, selectivity to benzene and toluene drops to zero as the temperature increases above 540 K. Over the complete temperature range, no selectivity to benzyl alcohol is observed.

Thus, the MKM predicts that the relative selectivity for toluene is the highest compared to those for all four products at low temperatures till 540 K, while the relative selectivity of benzaldehyde dominates at temperatures of 540 K and higher. With the O_{vac} (*) completely covered with adsorbed benzaldehyde (P_1^*) for the most part of the investigated temperature range (see Fig. S9b†), this switch in selectivity from toluene to benzaldehyde as the temperature increases is a direct consequence of benzaldehyde desorption being more activated than its further hydrogenation (see Fig. 6). In agreement with the current MKM study, the limited experimental data available for benzoic acid HDO on metal oxides (*i.e.*, ZrO_2, HfO_2, TiO_2) also report the production of toluene, benzene, and benzaldehyde at low temperatures and a steep increase in benzaldehyde selectivity as temperature increases.[6] Potential modifications in the entropy treatment and using an alternative pathway for benzaldehyde hydrogenation (as depicted in Fig. S4†) may affect the selectivity of benzene and toluene at low temperatures where the production rates are lower than 10^{-10} s^{-1} and the onset temperature where benzaldehyde becomes dominant (Fig. S10†). Nevertheless, the overall trend of

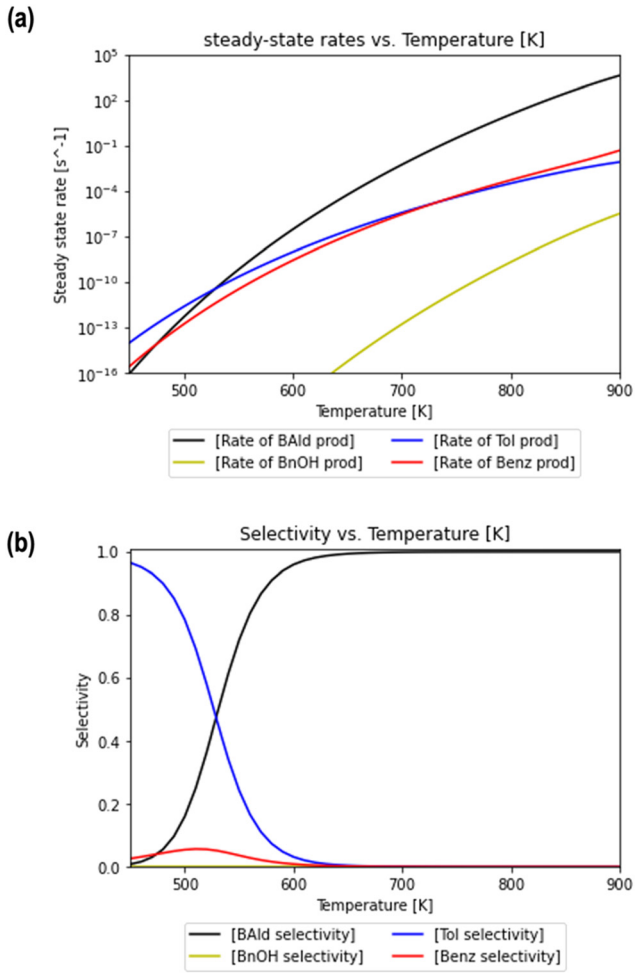

Fig. 8 Rates of formation and selectivity of products predicted through the microkinetic model. Steady state rates (a) of benzaldehyde (black), benzyl alcohol (blue circles), toluene (dashed red), and benzene (dotted green) production are plotted as a function of reaction temperature. The relative selectivity of each product (b) is calculated using rates of formation at steady state at various temperatures. The coverages of select surface intermediates at different temperatures are included in Fig. S9b.†

increase in benzaldehyde selectivity with increasing temperature remains consistent.

We further analyze the MKM using the degree of rate control at the crucial temperature of 540 K (Table 1, Fig. S11a†), where several products are observed. Almost all elementary steps contribute insignificantly to the overall reaction rate when perturbated, with a degree of rate control near zero. The reaction steps with the degree of rate control higher than 0.1 involve benzaldehyde desorption, decarbonylation *via* C–C bond cleavage and further hydrogenation to benzyl alcohol *via* hydride-mediated C–H bond formation. The results suggest that these elementary steps have significant impacts on the overall benzoic acid consumption. Additionally, the degree of selectivity control[71] quantifies how significantly each elementary step contributes to the relative increase in selectivity with respect to each product (Fig. S11b†).

The partial equilibrium index (PEI) is also calculated for each elementary step at 540 K (Table 1, Fig. S11c†). A majority of the elementary steps are not near equilibrium, which makes it difficult with PEI alone to pinpoint any one reaction that is the rate-determining step of the system. Eight elementary steps can be considered near-equilibrated with a PEI between 0.45 and 0.55. Contrarily, no steps have PEIs near zero, which would generally correspond to reactions with very low forward reaction rates. The PEI also confirms the results from the degree of rate control, namely that the reactions with a high degree of rate control are also far from equilibrium (*i.e.*, benzaldehyde desorption, decarbonylation, and further hydrogenation). In summary, the PEIs and degrees of rate control give a comprehensive overview of the microkinetic model and suggest which elementary steps should be targeted through rational catalyst design. For example, modifications to the catalyst that can alter the desorption, decarbonylation, or further hydrogenation of benzaldehyde (*i.e.*, the non-equilibrated elementary steps with the highest degree of rate control) are expected to have significant impacts on the overall reaction according to the microkinetic model. Though not represented mathematically in the MKM that predicts rate per vacancy site, promoting vacancy formation would also generate more active sites and enhance the rate.

4. Conclusions

C–H bond formation to four aromatic products (*i.e.*, benzaldehyde, benzyl alcohol, toluene, and benzene) on anatase TiO_2 (001) can occur through a hydride-mediated mechanism on surface O_{vac} sites. In this mechanism, a negatively charged monoanionic intermediate ligand reacts with a favorable reaction energy with a hydride coadsorbed in O_{vac}. The overall reaction energy diagram of benzoic acid hydrodeoxygenation was constructed using plausible intermediates and kinetic barriers related to C–H bond formation as well as decarboxylation and decarbonylation. Finally, a microkinetic model was constructed using the overall mechanism and DFT energetics. The MKM suggests that selectivity to toluene is favored over the other three products at low temperatures, while benzaldehyde selectivity dominates at moderate-to-high temperatures. Competing mechanisms such as those for benzaldehyde hydrogenation, decarbonylation, and desorption result in the model predicting different product formation rates and selectivities. MKM analysis through degree of rate control and partial equilibrium index calculations shows several elementary steps that are far from equilibrium and thus can be targeted in the future for potentially significant impacts on the overall rate and selectivity of benzoic acid hydrodeoxygenation.

Data availability

Data are available within the article and its ESI.†

Disclaimer

The views expressed herein do not necessarily represent the views of the U.S. Department of Energy or the United States Government.

Conflicts of interest

There are no conflicts to declare.

Acknowledgements

This material is based upon work supported by the U.S. Department of Energy's Office of Energy Efficiency and Renewable Energy (EERE) under the Advanced Manufacturing Office Award Number DE-EE0007897 awarded to the REMADE Institute, a division of Sustainable Manufacturing Innovation Alliance Corp. Computational resources were provided through the Extreme Science and Engineering Discovery Environment (XSEDE), supported by the National Science Foundation (grant no. ACI-1548562).

References

1 N. Perret, X. Wang, J. J. Delgado, G. Blanco, X. Chen, C. M. Olmos, S. Bernal and M. A. Keane, Selective Hydrogenation of Benzoic Acid over Au Supported on CeO2 and Ce0.62Zr0.38O2: Formation of Benzyl Alcohol, *J. Catal.*, 2014, **317**, 114–125, DOI: **10.1016/j.jcat.2014.06.010**.

2 X. Chen, Z. Wang, H. Daly, R. Morgan, H. Manyar, C. Byrne, A. S. Walton, S. F. R. Taylor, M. Smith, R. Burch, P. Hu and C. Hardacre, Hydrogenation of Benzoic Acid to Benzyl Alcohol over Pt/SnO2, *Appl. Catal., A*, 2020, **593**, 117420, DOI: **10.1016/j.apcata.2020.117420**.

3 J. Pritchard, G. A. Filonenko, R. Van Putten, E. J. M. Hensen and E. A. Pidko, Heterogeneous and Homogeneous Catalysis for the Hydrogenation of Carboxylic Acid Derivatives: History, Advances and Future Directions, *Chem. Soc. Rev.*, 2015, 3808–3833, DOI: **10.1039/c5cs00038f**.

4 B. Chen, U. Dingerdissen, J. G. E. Krauter, H. G. J. Lansink Rotgerink, K. Möbus, D. J. Ostgard, P. Panster, T. H. Riermeier, S. Seebald, T. Tacke and H. Trauthwein, New Developments in Hydrogenation Catalysis Particularly in Synthesis of Fine and Intermediate Chemicals, *Appl. Catal., A*, 2005, **280**(1), 17–46, DOI: **10.1016/j.apcata.2004.08.025**.

5 M. W. De Lange, J. G. Van Ommen and L. Lefferts, Deoxygenation of Benzoic Acid on Metal Oxides: 1. The Selective Pathway to Benzaldehyde, *Appl. Catal., A*, 2001, **220**(1–2), 41–49.

6 C. A. Koutstaal and V. Ponec, New Aspects of the Selective Reduction of Aromatic Carboxylic Acids to the Aldehydes, *Science and technology in catalysis*, 1994, pp. 105–110.

7 C. Ozdemir, S. Şahinkaya, E. Kalıpcı, M. K. Oden, Ö. Çepelioğullar and A. E. Pütün, Utilization of Two Different Types of Plastic Wastes from Daily and Industrial Life, *Journal of Selcuk University Natural and Applied Science*, 2013, **2**(2), 694–706.

8 S. D. Anuar Sharuddin, F. Abnisa, W. M. A. Wan Daud and M. K. Aroua, A Review on Pyrolysis of Plastic Wastes, *Energy Convers. Manage.*, 2016, 308–326, DOI: **10.1016/j.enconman.2016.02.037**.

9 Y. Sakata, C. A. Van Tol-Koutstaal and V. Ponec, Selectivity Problems in the Catalytic Deoxygenation of Benzoic Acid, *J. Catal.*, 1997, **169**(1), 13–21.

10 J. Li, J. Zhang, S. Wang, G. Xu, H. Wang and D. G. Vlachos, Chemoselective Hydrodeoxygenation of Carboxylic Acids to Hydrocarbons over Nitrogen-Doped Carbon-Alumina Hybrid Supported Iron Catalysts, *ACS Catal.*, 2019, **9**(2), 1564–1577, DOI: **10.1021/acscatal.8b04967**.

11 J. Ullrich and B. Breit, Selective Hydrogenation of Carboxylic Acids to Alcohols or Alkanes Employing a Heterogeneous Catalyst, *ACS Catal.*, 2018, **8**(2), 785–789, DOI: **10.1021/acscatal.7b03484**.

12 T. Yokoyama, T. Setoyama, N. Fujita, M. Nakajima, T. Maki and K. Fujii, Novel Direct Hydrogenation Process of Aromatic Carboxylic Acids to the Corresponding Aldehydes with Zirconia Catalyst, *Appl. Catal., A*, 1992, **88**(2), 149–161.

13 D. D. Poondi, The Influence of Metal-Support Interactions on the Hydrogenation Activity and Selectivity of Benzene-Toluene Mixtures, Benzaldehyde, and Phenylacetaldehyde, *PhD thesis*, The Pennsylvania State University, 1996.

14 D. Haffad, U. Kameswari, M. M. Bettahar, A. Chambellan and J. C. Lavalley, Reduction of Benzaldehyde on Metal Oxides, *J. Catal.*, 1997, **172**(1), 85–92.

15 A. Ausavasukhi, T. Sooknoi and D. E. Resasco, Catalytic Deoxygenation of Benzaldehyde over Gallium-Modified ZSM-5 Zeolite, *J. Catal.*, 2009, **268**(1), 68–78, DOI: **10.1016/j.jcat.2009.09.002**.

16 Y. Hao, C. Pischetola, F. Cárdenas-Lizana and M. A. Keane, Selective Liquid Phase Hydrogenation of Benzaldehyde to Benzyl Alcohol Over Alumina Supported Gold, *Catal. Lett.*, 2020, **150**(3), 881–887, DOI: **10.1007/s10562-019-02944-y**.

17 S. T. King and E. J. Strojny, An in Situ Study of Methyl Benzoate and Benzoic Acid Reduction on Yttrium Oxide by Infrared Spectroscopic Flow Reactor, *J. Catal.*, 1982, **76**(2), 274–284.

18 M. A. Vannice and D. Poondi, The Effect of Metal-Support Interactions on the Hydrogenation of Benzaldehyde and Benzyl Alcohol, *J. Catal.*, 1997, **169**(1), 166–175.

19 J. T. Bhanushali, I. Kainthla, R. S. Keri and B. M. Nagaraja, Catalytic Hydrogenation of Benzaldehyde for Selective Synthesis of Benzyl Alcohol: A Review, *ChemistrySelect*, 2016, 3839–3853, DOI: **10.1002/slct.201600712**.

20 B. Nair, Final Report on the Safety Assessment of Benzyl Alcohol, Benzoic Acid, and Sodium Benzoate, *Int. J. Toxicol.*, 2001, **20**(3), 23–50, DOI: **10.1080/10915810152630729**.

21 F. Pinna, F. Menegazzo, M. Signoretto, P. Canton, G. Fagherazzi and N. Pernicone, Consecutive Hydrogenation of Benzaldehyde over Pd Catalysts Influence of Supports and Sulfur Poisoning, *Appl. Catal., A*, 2001, **219**(1–2), 195–200.

22 M. Tang, S. Mao, M. Li, Z. Wei, F. Xu, H. Li and Y. Wang, RuPd Alloy Nanoparticles Supported on N-Doped Carbon as an Efficient and Stable Catalyst for Benzoic Acid Hydrogenation, *ACS Catal.*, 2015, **5**(5), 3100–3107, DOI: **10.1021/acscatal.5b00037**.

23 X. Xu, M. Tang, M. Li, H. Li and Y. Wang, Hydrogenation of Benzoic Acid and Derivatives over Pd Nanoparticles

Supported on N-Doped Carbon Derived from Glucosamine Hydrochloride, *ACS Catal.*, 2014, **4**(9), 3132–3135, DOI: **10.1021/cs500859n**.

24 M. Guo, X. Kong, C. Li and Q. Yang, Hydrogenation of Benzoic Acid Derivatives over Pt/TiO2 under Mild Conditions, *Commun. Chem.*, 2021, **4**(1), 54, DOI: **10.1038/s42004-021-00489-z**.

25 H. Zhang, J. Dong, X. Qiao, J. Qin, H. Sun, A. Wang, L. Niu and G. Bai, In-Situ Generated Highly Dispersed Nickel Nanoclusters Confined in MgAl Mixed Metal Oxide Platelets for Benzoic Acid Hydrogenation, *J. Catal.*, 2019, **372**, 258–265, DOI: **10.1016/j.jcat.2019.03.012**.

26 S. B. Shinde and R. M. Deshpande, Catalytic Hydrogenation of Benzoic Acid, in *New Advances in Hydrogenation Processes - Fundamentals and Applications*, InTech, 2017, DOI: **10.5772/66428**.

27 N. Perret, F. Cárdenas-Lizana and M. A. Keane, Selective Hydrogenation of Benzaldehyde to Benzyl Alcohol over Au/Al 2O3, *Catal. Commun.*, 2011, **16**(1), 159–164, DOI: **10.1016/j.catcom.2011.09.017**.

28 Y. Sakata and V. Ponec, Reduction of Benzoic Acid on CeO2 and, the Effect of Additives, *Appl. Catal., A*, 1998, **166**, 173–184.

29 P. Mars and D. W. Van Krevelen, Oxidations Carried out by Means of Vanadium Oxide Catalysts, *Chem. Eng. Sci.*, 1954, **3**, 41–59.

30 A. Wang, J. Li and T. Zhang, Heterogeneous Single-Atom Catalysis, *Nat. Rev. Chem.*, 2018, 65–81, DOI: **10.1038/s41570-018-0010-1**.

31 M. T. Darby, M. Stamatakis, A. Michaelides and E. C. H. Sykes, Lonely Atoms with Special Gifts: Breaking Linear Scaling Relationships in Heterogeneous Catalysis with Single-Atom Alloys, *J. Phys. Chem. Lett.*, 2018, 5636–5646, DOI: **10.1021/acs.jpclett.8b01888**.

32 K. Liu, P. Yan, H. Jiang, Z. Xia, Z. Xu, S. Bai and Z. C. Zhang, Silver Initiated Hydrogen Spillover on Anatase TiO2 Creates Active Sites for Selective Hydrodeoxygenation of Guaiacol, *J. Catal.*, 2019, **369**, 396–404, DOI: **10.1016/j.jcat.2018.11.033**.

33 J. Hu, E. M. Kim, M. J. Janik and K. Alexopoulos, Hydrogen Activation and Spillover on Anatase TiO2-Supported Ag Single-Atom Catalysts, *J. Phys. Chem. C*, 2022, **126**(17), 7482–7491, DOI: **10.1021/acs.jpcc.2c01670**.

34 W. C. Conner and J. L. Falconer, Spillover in Heterogeneous Catalysis, *Chem. Rev.*, 1995, **95**, 759–788.

35 X. He, Q. He, Y. Deng, M. Peng, H. Chen, Y. Zhang, S. Yao, M. Zhang, D. Xiao, D. Ma, B. Ge and H. Ji, A Versatile Route to Fabricate Single Atom Catalysts with High Chemoselectivity and Regioselectivity in Hydrogenation, *Nat. Commun.*, 2019, **10**(1), 3663, DOI: **10.1038/s41467-019-11619-6**.

36 G. Kyriakou, M. B. Boucher, A. D. Jewell, E. A. Lewis, T. J. Lawton, A. E. Baber, H. L. Tierney, M. Flytzani-Stephanopoulos and E. C. H. Sykes, Isolated Metal Atom Geometries as a Strategy for Selective Heterogeneous Hydrogenations, *Science*, 2012, **335**(6073), 1209–1212.

37 X. Pan, M. Q. Yang, X. Fu, N. Zhang and Y. J. Xu, Defective TiO2 with Oxygen Vacancies: Synthesis, Properties and Photocatalytic Applications, *Nanoscale*, 2013, 3601–3614, DOI: **10.1039/c3nr00476g**.

38 R. Schaub, E. Wahlström, A. Rønnau, E. Lægsgaard, I. Stensgaard and F. Besenbacher, Oxygen-Mediated Diffusion of Oxygen Vacancies on the TiO2(110) Surface, *Science*, 2003, **299**, 377–379, DOI: **10.1126/science.1059133**.

39 K. Liu, G. Hou, P. Gao, X. Nie, S. Bai, M. J. Janik and Z. C. Zhang, Evolution of Multiple Spillover Hydrogen Species on Anatase Titanium Dioxide, *Cell Rep. Phys. Sci.*, 2022, **3**(12), 101190, DOI: **10.1016/j.xcrp.2022.101190**.

40 X. Han, Q. Kuang, M. Jin, Z. Xie and L. Zheng, Synthesis of Titania Nanosheets with a High Percentage of Exposed (001) Facets and Related Photocatalytic Properties, *J. Am. Chem. Soc.*, 2009, **131**(9), 3152–3153, DOI: **10.1021/ja8092373**.

41 O. Carp, C. L. Huisman and A. Reller, Photoinduced Reactivity of Titanium Dioxide, *Prog. Solid State Chem.*, 2004, 33–177, DOI: **10.1016/j.progsolidstchem.2004.08.001**.

42 U. Diebold, The Surface Science of Titanium Dioxide, *Surf. Sci. Rep.*, 2003, **48**(5–8), 53–229.

43 G. te Velde, F. M. Bickelhaupt, E. J. Baerends, C. Fonseca Guerra, S. J. A. van Gisbergen, J. G. Snijders and T. Ziegler, Chemistry with ADF, *J. Comput. Chem.*, 2001, **22**(9), 931–967, DOI: **10.1002/jcc.1056**.

44 G. Pacchioni, Oxygen Vacancy: The Invisible Agent on Oxide Surfaces, *ChemPhysChem*, 2003, 1041–1047, DOI: **10.1002/cphc.200300835**.

45 T. L. Thompson and J. T. Yates, TiO2-Based Photocatalysis: Surface Defects, Oxygen and Charge Transfer, *Top. Catal.*, 2005, 197–210, DOI: **10.1007/s11244-005-3825-1**.

46 A. Roldán, M. Boronat, A. Corma and F. Illas, Theoretical Confirmation of the Enhanced Facility to Increase Oxygen Vacancy Concentration in TiO2 by Iron Doping, *J. Phys. Chem. C*, 2010, **114**(14), 6511–6517, DOI: **10.1021/jp911851h**.

47 G. Kresse and J. Furthmüller, Efficient Iterative Schemes for Ab Initio Total-Energy Calculations Using a Plane-Wave Basis Set, *Phys. Rev. B*, 1996, **54**(16), 11169.

48 J. P. Perdew, K. Burke and M. Ernzerhof, Generalized Gradient Approximation Made Simple, *Phys. Rev. Lett.*, 1996, **77**(18), 3865.

49 P. E. Blochl, Projector Augmented-Wave Method, *Phys. Rev. B*, 1994, **50**(24), 17953.

50 S. Grimme, J. Antony, S. Ehrlich and H. Krieg, A Consistent and Accurate Ab Initio Parametrization of Density Functional Dispersion Correction (DFT-D) for the 94 Elements H-Pu, *J. Chem. Phys.*, 2010, **132**(15), 154104, DOI: **10.1063/1.3382344**.

51 W. Heckel, T. Würger, S. Müller and G. Feldbauer, Van Der Waals Interaction Really Matters: Energetics of Benzoic Acid on TiO2 Rutile Surfaces, *J. Phys. Chem. C*, 2017, **121**(32), 17207–17214, DOI: **10.1021/acs.jpcc.7b03149**.

52 V. I. Anisimov, J. Zaanen and O. K. Andersen, Band Theory and Mott Insulators: Hubbard U Instead of Stoner I, *Phys. Rev. B*, 1991, **44**(3), 943.

53 Z. Hu and H. Metiu, Choice of U for DFT+U Calculations for Titanium Oxides, *J. Phys. Chem. C*, 2011, **115**(13), 5841–5845, DOI: **10.1021/jp111350u**.

54 H. J. Monkhorst and J. D. Pack, Special Points for Brillonin-Zone Integrations, *Phys. Rev. B: Solid State*, 1976, **13**(12), 5188–5192.
55 H. V. Thang, G. Pacchioni, L. DeRita and P. Christopher, Nature of Stable Single Atom Pt Catalysts Dispersed on Anatase TiO2, *J. Catal.*, 2018, **367**, 104–114, DOI: **10.1016/j.jcat.2018.08.025**.
56 V. Vorotnikov, S. Wang and D. G. Vlachos, Group Additivity for Estimating Thermochemical Properties of Furanic Compounds on Pd(111), *Ind. Eng. Chem. Res.*, 2014, **53**(30), 11929–11938, DOI: **10.1021/ie502049a**.
57 P. J. Linstrom and W. G. Mallard, The NIST Chemistry WebBook: A Chemical Data Resource on the Internet, *J. Chem. Eng. Data*, 2001, **46**(5), 1059–1063, DOI: **10.1021/je000236i**.
58 V. Diky, C. Muzny, A. Smolyanitsky, A. Bazyleva, R. D. Chirico, J. W. Magee, E. Paulechka, A. F. Kazakov, S. Townsend, E. Lemmon, M. D. Frenkel and K. Kroenlein, *ThermoData Engine (TDE) Version 10 (Pure Compounds, Binary Mixtures, Ternary Mixtures, and Chemical Reactions): NIST Standard Reference Database 103b*, National Institute of Standards and Technology, Gaithersburg, MD, 2015.
59 C. L. Yaws, *Yaws' Handbook of Thermodynamic and Physical Properties of Chemical Compounds*, Knovel, 2003.
60 C. T. Campbell and J. R. V. Sellers, The Entropies of Adsorbed Molecules, *J. Am. Chem. Soc.*, 2012, **134**(43), 18109–18115, DOI: **10.1021/ja3080117**.
61 Y. P. Li, J. Gomes, S. M. Sharada, A. T. Bell and M. Head-Gordon, Improved Force-Field Parameters for QM/MM Simulations of the Energies of Adsorption for Molecules in Zeolites and a Free Rotor Correction to the Rigid Rotor Harmonic Oscillator Model for Adsorption Enthalpies, *J. Phys. Chem. C*, 2015, **119**(4), 1840–1850, DOI: **10.1021/jp509921r**.
62 M. A. Vannice, S. H. Hyun, B. Kalparci and W. C. Liauh, Entropies of Adsorption in Heterogeneous Catalytic Reactions, *J. Catal.*, 1979, **56**(3), 358–362.
63 A. H. Motagamwala and J. A. Dumesic, Microkinetic Modeling: A Tool for Rational Catalyst Design, *Chem. Rev.*, 2021, 1049–1076, DOI: **10.1021/acs.chemrev.0c00394**.
64 A. A. Gokhale, S. Kandoi, J. P. Greeley, M. Mavrikakis and J. A. Dumesic, Molecular-Level Descriptions of Surface Chemistry in Kinetic Models Using Density Functional Theory, *Chem. Eng. Sci.*, 2004, **59**, 4679–4691, DOI: **10.1016/j.ces.2004.09.038**.
65 H. Eyring, The Activated Complex in Chemical Reactions, *J. Chem. Phys.*, 1935, **3**(2), 63–71, DOI: **10.1063/1.1749604**.
66 H. Eyring, The Activated Complex And The Absolute Rate Of Chemical Reactions, *Chem. Rev.*, 1935, **17**(1), 65–77.
67 J. D. Kammert, A. Chemburkar, N. Miyake, M. Neurock and R. J. Davis, Reaction Kinetics and Mechanism for the Catalytic Reduction of Propionic Acid over Supported ReO XPromoted by Pd, *ACS Catal.*, 2021, **11**(3), 1435–1455, DOI: **10.1021/acscatal.0c04328**.
68 L. A. Gomez, C. Q. Bavlnka, T. E. Zhang, D. E. Resasco and S. P. Crossley, Revealing the Mechanistic Details for the Selective Deoxygenation of Carboxylic Acids over Dynamic MoO3 Catalysts, *ACS Catal.*, 2023, **13**(13), 8455–8466, DOI: **10.1021/acscatal.3c01053**.
69 E. A. Solano Espinoz and W. E. Vallejo Narváez, Density Functional Theory and RRKM Calculations of Decompositions of the Metastable E-2,4-pentadienalmolecular Ions, *J. Mass Spectrom.*, 2010, **45**(7), 722–733, DOI: **10.1002/jms.1760**.
70 C. T. Campbell, The Degree of Rate Control: A Powerful Tool for Catalysis Research, *ACS Catal.*, 2017, 2770–2779, DOI: **10.1021/acscatal.7b00115**.
71 C. T. Campbell, Micro- and Macro-kinetics: Their Relationship in Heterogeneous Catalysis, *Top. Catal.*, 1994, **1**, 353–366.
72 G. R. Wittreich, K. Alexopoulos and D. G. Vlachos, Microkinetic Modeling of Surface Catalysis, in *Handbook of Materials Modeling: Applications: Current and Emerging Materials*, Springer International Publishing, 2nd edn, 2020, pp. 1377–1404, DOI: **10.1007/978-3-319-44680-6_5**.
73 A. Samant and D. G. Vlachos, Overcoming Stiffness in Stochastic Simulation Stemming from Partial Equilibrium: A Multiscale Monte Carlo Algorithm, *J. Chem. Phys.*, 2005, **123**(14), 144114, DOI: **10.1063/1.2046628**.
74 A. G. Thomas, W. R. Flavell, A. K. Mallick, A. R. Kumarasinghe, D. Tsoutsou, N. Khan, C. Chatwin, S. Rayner, G. C. Smith, R. L. Stockbauer, S. Warren, T. K. Johal, S. Patel, D. Holland, A. Taleb and F. Wiame, Comparison of the Electronic Structure of Anatase and Rutile TiO2 Single-Crystal Surfaces Using Resonant Photoemission and X-Ray Absorption Spectroscopy, *Phys. Rev. B: Condens. Matter Mater. Phys.*, 2007, **75**(3), 035105, DOI: **10.1103/PhysRevB.75.035105**.
75 M. Buchholz, M. Xu, H. Noei, P. Weidler, A. Nefedov, K. Fink, Y. Wang and C. Wöll, Interaction of Carboxylic Acids with Rutile TiO2(110): IR-Investigations of Terephthalic and Benzoic Acid Adsorbed on a Single Crystal Substrate, *Surf. Sci.*, 2016, **643**, 117–123, DOI: **10.1016/j.susc.2015.08.006**.
76 Q. Guo, I. Cocks and E. M. Williams, The Adsorption of Benzoic Acid on a TiO2(110) Surface Studied Using STM, ESDIAD and LEED, *Surf. Sci.*, 1997, **393**(1–3), 1–11.
77 N. Martsinovich, D. R. Jones and A. Troisi, Electronic Structure of TiO2 Surfaces and Effect of Molecular Adsorbates Using Different DFT Implementations, *J. Phys. Chem. C*, 2010, **114**(51), 22659–22670, DOI: **10.1021/jp109756g**.
78 S. P. Bates, G. Kresse and M. J. Gillan, The Adsorption and Dissociation of ROH Molecules on TiO2(110), *Surf. Sci.*, 1998, **409**(2), 336–349.
79 P. Persson, R. Bergstrom and S. Lunell, Quantum Chemical Study of Photoinjection Processes in Dye-Sensitized TiO2 Nanoparticles, *J. Phys. Chem. B*, 2000, **104**(44), 10348–10351, DOI: **10.1021/jp002550p**.
80 G. Tabacchi, M. Fabbiani, L. Mino, G. Martra and E. Fois, The Case of Formic Acid on Anatase TiO2(101): Where Is the Acid Proton?, *Angew. Chem., Int. Ed.*, 2019, **58**(36), 12431–12434, DOI: **10.1002/anie.201906709**.
81 L. Xue, W. Su and Z. Lin, Mechanism of Silver- and Copper-Catalyzed Decarboxylation Reactions of Aryl Carboxylic Acids, *Dalton Trans.*, 2011, **40**(44), 11926–11936, DOI: **10.1039/c1dt10771b**.

82 L. J. Gooßen, N. Rodríguez, C. Linder, P. P. Lange and A. Fromm, Comparative Study of Copper- and Silver-Catalyzed Protodecarboxylations of Carboxylic Acids, *ChemCatChem*, 2010, **2**(4), 430–442, DOI: **10.1002/cctc.200900277**.

83 Q. Jin, J. Li, A. Ariafard, A. J. Canty and R. A. J. O'Hair, Substituent Effects in the Decarboxylation Reactions of Coordinated Arylcarboxylates in Dinuclear Copper Complexes, [(Napy)Cu2(O2CC6H4X)]+†, *Eur. J. Mass Spectrom.*, 2017, **23**(6), 351–358, DOI: **10.1177/1469066717729067**.

84 M. John, K. Alexopoulos, M. F. Reyniers and G. B. Marin, Mechanistic Insights into the Formation of Butene Isomers from 1-Butanol in H-ZSM-5: DFT Based Microkinetic Modelling, *Catal. Sci. Technol.*, 2017, **7**(5), 1055–1072, DOI: **10.1039/c6cy02474b**.

85 M. Saunders and M. R. Kates, Rates of Degenerate 1,2-Hydride and 1,2-Methide Shifts from the Carbon-13 Nuclear Magnetic Resonance Spectra of Tertiary Alkyl Cations, *J. Am. Chem. Soc.*, 1978, **100**(2), 7082–7083.

86 L. Zhang, M. Zhou, A. Wang and T. Zhang, Selective Hydrogenation over Supported Metal Catalysts: From Nanoparticles to Single Atoms, *Chem. Rev.*, 2020, 683–733, DOI: **10.1021/acs.chemrev.9b00230**.